Fluorescence Lifetime Heterogeneity Resolution in the Frequency Domain by Lifetime Moments Analysis

Alessandro Esposito,*† Hans C. Gerritsen,† and Fred S. Wouters*
*Cell Biophysics Group, European Neuroscience Institute, 37073 Göttingen, Germany; and †Debye Institute, Utrecht University, Utrecht, The Netherlands

ABSTRACT Fluorescence lifetime imaging microscopy presents a powerful tool in biology and biophysics because it allows the investigation of the local environment of a fluorochrome in living cells in a quantitative manner. Furthermore, imaging Förster-type resonance energy transfer (FRET) by fluorescence lifetime imaging microscopy enables protein-protein interactions and intermolecular distances to be mapped under physiological conditions. Quantitative and precise data analysis methods are required to access the richness of information that is contained in FRET data on biological samples. Lifetime detection in the frequency-domain yields two lifetime estimations. The lifetime moments analysis (LiMA) provides a quantitative measure of the lifetime distribution broadness by exploiting the analytical relationship between the phase- and demodulation-lifetime estimations and relating them to the weighted average and variance of the lifetime distribution. The LiMA theoretical framework is validated by comparison with global analysis and by applying it to a constrained two-component FRET system using simulations and experiments. Furthermore, a novel LIMA-based error analysis and a more intuitive formalism for global analysis are presented. Finally, a new method to resolve a FRET system is proposed and experimentally applied to the investigation of protein-protein interactions.

INTRODUCTION

The fluorescence lifetime is a spectroscopic property of a fluorochrome that is sensitive to its chemical-physical environment. The first lifetime measurements were performed by E. Gaviola (1) in the 1920s using phase fluorimetry. This technique and its theoretical background were developed and expanded by the group of G. Weber (2) in the following years. The advances in technology in both frequency (3) and time (4) domain in the 1980s eventually resulted in the development of lifetime detection in microscopy. A large variety of systems has been developed based on different frequency- and time-domain wide-field approaches (5–9) and laser scanning approaches (10–15).

Fluorescence lifetime imaging microscopy (FLIM) is a powerful tool to, for instance, enhance contrast in samples with more than one fluorochrome, quantify ion concentration, and detect Förster-type resonance energy transfer (FRET). The analysis of lifetime heterogeneity may yield important information about photophysical processes (16,17) and can be used to derive estimators for, e.g., average lifetime and FRET efficiency (this work). FRET is a quantum-physical process that causes nonradiative transfer of excitation energy between two chromophores by dipole-dipole coupling (18,19). In this process, the acceptor fluorescence emission is enhanced at the cost of donor quantum yield and the donor lifetime is decreased (20,21). This is due to the fact that the donor photophysics is coupled to the acceptor and an additional depopulation pathway is provided by FRET. FLIM is increasingly used to study FRET in biological systems because it allows the construction of an interaction map of biomolecules inside cells (22,23). Because of the extreme distance dependence of FRET, two biomolecules labeled with suitable fluorochromes that undergo FRET have to physically interact.

Detection in the frequency domain (FD) using a sinusoidally modulated light source and a detector modulated at the same frequency, presents a robust technique for the measurement of fluorescence lifetimes (8,24). The detector acquires images at different phase delays relative to the excitation light and the resulting phase-dependent image stack is fitted to a sine function or analyzed by first component Fourier analysis to retrieve lifetimes (25).

FD-FLIM provides two lifetime estimations from the analysis of the demodulation and phase-lag between a reference measurement and the sample. Usually these two lifetimes are referred to as being independent. However, whether they are truly independent is debatable. The modulation lifetime is in general greater than or equal to the phase lifetime (8,26–28). The two estimations are only identical for a sample exhibiting a monoexponential decay. The experimental observation that the two estimations diverge at growing sample lifetime heterogeneity has been reported repeatedly in literature, however, without a clear theoretical explanation or analytical solution. The formalism presented here aims at lifetime heterogeneity analysis and does not take into account excited-state reactions that may invert the two lifetime estimations (26,29).

FLIM can be used to detect FRET by determining the reduction of the donor lifetime. In the simplest case, two

Submitted September 24, 2004, and accepted for publication August 22, 2005.

Address reprint requests to Alessandro Esposito, Waldweg 33, 37073 Göttingen, Germany. Tel.: 49-551-3912356; Fax: 49-551-3912346; E-mail: aesposito@quantitative-microscopy.org.

0006-3495/05/12/4286/14 $2.00

doi: 10.1529/biophysj.104.053397

lifetimes are present in each pixel; one from the donor molecules that do not undergo FRET and one from the donor molecules that undergo FRET. Now, the quantification of the FRET efficiency between the interacting components requires knowledge about the amount of noninteracting donor molecules that exhibit no FRET. Attempts to resolve the two real lifetimes from the two estimated values were typically not followed as this requires knowledge of the relative weight of the two components.

In the recent years, global analysis (GA) methods were described (30,31) that aim at extracting this quantitative information. These methods rely on the assumption that two spatially invariant fluorescence lifetimes are present in the specimen. The invariance property suffices for single-frequency resolution of the two lifetime components for each pixel.

Here, we present:

1. an analytical solution of the relationship between the modulation- and phase-lifetime estimations. This discloses the simple physical background underneath the divergence of the two estimations and allows the computation of additional relevant quantities such as pixel-by-pixel estimators for the decay time variance and average lifetime.
2. a more descriptive physical explanation of single-frequency global analysis and its graphical representation (32) for a two-component system. In addition, the frequency limits are investigated.
3. the analysis of a constrained two-component system exhibiting FRET (33) with the derivation of its noise sensitivity and a new robust FRET estimator.

The presented theoretical framework is validated by in vitro experiments on mixtures of fluorescent proteins. LiMA was able to predict and quantify the lifetime heterogeneity of these samples. Furthermore, the experimental comparison of the method with lifetime detection in the time domain (TD) is presented. Here, fitting the time-resolved fluorescence decays gives quantitative information about the lifetime heterogeneities. Moreover, we illustrate the application of LiMA to a relevant biological case, i.e., the quantification of FRET between fluorochromes resident in lipid microdomains. The experimental data are compared with computer simulation to further confirm the results.

MATERIAL AND METHODS

Microscopy

The frequency-domain FLIM is an in-house-developed system built around a fully automated Axiovert200M microscope (Carl Zeiss Jena GmbH, Jena, Germany). The excitation light is provided by an Innova 300C Argon laser (Coherent, Santa Clara, CA) whose 488- and 514-nm lines were used for excitation of the green fluorescent protein (EGFP, Clontech, Palo Alto, CA) and two EYFP mutants. The laser beam is intensity modulated by an acousto-optic modulator ME405 (AOM, IntraAction, Bellwood, IL) and the first-order sine-like modulated output is selected by an iris. The laser is further attenuated by a variable neutral density filter disk and focused on a continuously vibrated (50 Hz) fiber-optic cable to remove speckle noise. The despeckled laser beam is expanded by a concave lens onto the back input port of the microscope. Fluorescence detection is performed by an ImagerQE CCD connected to the output phosphor screen of a ''High-Range Imager'' multichannel plate (MCP) intensifier, both by Lavision GmbH (Göttingen, Germany). An Imager Compact camera (Lavision GmbH) installed on a second output port provides high-resolution intensity images of the sample. The MCP gain and the AOM are driven by two phase-locked high-stability signal generators IFR2023A (IFR System, Aeroflex, Plainview, NY) at a modulation frequency equal to 80.08 MHz with 16 phase-steps.

The time-domain FLIM experiments were carried out on a two-photon laser scanning microscope that is based on a Mira900 mode-locked femtosecond Ti:Sapphire, pumped by a Verdi-V8 laser (both Coherent), and a TSC SP2 AOBS confocal microscope (Leica Microsystems Heidelberg GmbH, Mannheim, Germany). A custom-made filter wheel is connected to the output port of the scanning head and to the TD-FLIM detector, a MCP-PMT (R3809U-50 by Hamamatsu Photonics, Sunayama-cho, Japan). The time-resolved fluorescence decays are acquired by time-correlated single-photon counting using a SPC830 acquisition board and SPC-IMAGE software (Becker & Hickl GmbH, Berlin, Germany). The excitation of EGFP by two-photon absorption was accomplished by tuning the laser to 900 nm.

The EGFP, EYFPs, and Alexa-594 fluorescence intensities were imaged using bandpass filters 515/15 (peak wavelength/broadness in nanometers), 535/30 and 610/75, respectively (AHF Analysentechnik AG, Tübingen, Germany).

FD-FLIM calibration

The calibration of the FD-FLIM is crucial to obtain the optimal measurement of the two lifetime estimations.

Zero lifetime calibrations were performed by imaging a mirror positioned in the sample plane using a filter cube without filters. Subsequent time drifts of the calibration parameters were continuously corrected using a scattering reference positioned at the automated reflector turret of the microscope. The automation of this standard procedure grants high stability and reproducibility of the measurements, but the calibration is performed without the EGFP filter set. To compensate for the fixed phase delay that the filter introduces (28) we estimated this parameter by measuring the EGFP lifetimes through one or two copies of the same filter. The difference (0.032 radians at 80.08 MHz modulation frequency) was taken into account in the analysis and is comparable with other estimations of filter insertion phase delays using other procedures (28). Phase-dependent images were acquired by gating the MCP with 1000 ps gating width or using a direct radio-frequency modulation of the MCP gain. The presented data did not differ between acquisition modes. In the following section, RF-mode phase-stacks are presented because this approach has the highest photon collection efficiency.

Data analysis

The data collected in the frequency domain were analyzed by first-component Fourier analysis (25). Photobleaching correction (33) was performed by averaging a phase-stack acquired at incremental phase delays with a stack acquired using a reverse phase protocol. During the writing of this manuscript an improved method for photobleaching correction was published (34). In our experiments, each image of the phase-stack was smoothed (averaging 3×3 kernel). This procedure did not affect the lifetimes in the images. Further LiMA analysis was performed using a custom-developed Matlab (Mathwork, Natick, MA) toolbox ''ImFluo'' that can be downloaded from the internet (www.quantitative-microscopy.org/pub/lima.html). The image phase-stack was processed by first component Fourier analysis in which sine ($F_{\sin}$) and cosine ($F_{\cos}$) transforms of the image and the DC component (F_{DC}) were computed. The phase and the demodulation lifetimes were estimated using:

$$x_\phi = F_{\sin}F_{\cos}^{-1}; \quad x_m = \left[F_{DC}^2\left(F_{\cos}^2 + F_{\sin}^2\right)^{-1} - 1\right]^{\frac{1}{2}}. \qquad (1a, b)$$

The results of the Fourier analyses were always verified by direct fitting to a sine function.

The time-domain data was fitted to single-exponential or constrained double-exponential decays with SPC-IMAGE, whereas the stretched exponentials were fitted using ImFluo. Both the results were analyzed using the ImFluo toolbox. The stretched-exponential function, the relationships used to estimate the average lifetime, and its coefficient of variation are given in the Supplementary Material and are described in more details by Lee et al. (35). The time-domain data were always binned to reach an average photon count between 20,000 and 30,000 per pixel, allowing double-exponential fitting.

The global analysis and LiMA fits were performed by linear regression both with and without data weighing (31,32). The errors in the fitted quantities were computed by error propagation (see Supplementary Material). The errors in the modulation and phase estimates were computed as the uncertainty of the fit parameters in the phase-stack analysis. Unless otherwise specified, results from the nonweighed fits are presented.

Sample preparation

Carboxyl functionalized silica particles (PSi-20COOH) (20 μm) were purchased from G. Kisker GbR (Steinfurt, Germany) and covalently conjugated with a recombinantly produced EGFP-Tau fusion protein. The Tau protein is a natively unfolded protein that represents a good substrate for chemical labeling. The protein was produced using expression in Bl21DE3 bacteria from a pRSET-B (Invitrogen, Carlsbad, CA) expression construct and purified by hexahistidine-immobilized metal affinity chromatography (Talon resin by Clontech) according to the procedure provided by the supplier. Beads (1 ml) from the original stock was washed and resuspended in 1.2 ml MES buffer (50 mM, pH = 6.1). EGFP-Tau was cross linked to the beads by the derivatization of the carboxyl groups to yield amine-reactive succinimide ester groups by addition of 150 μl of *N*-hydroxy succinimide (100 mM) and 100 μl of 1-[3-(dimethylamino)propyl]-3-ethylcarbodiimide (50 mM). The sample was incubated while rotating at room temperature for 15′ after which 2.8 μl of β-mercaptoethanol was added to quench the reaction. After incubating for 10′, the beads were washed three times with MES for 5′ and resuspended with 900 μl EGFP-Tau (9 μM) in bicine buffer (bicine 50 mM, NaCl 100 mM, EGTA 1 mM, pH = 8.3). The particles were incubated with the protein solution while rotating for 20′ at room temperature followed by an overnight incubation at 4°C. The sample was subsequently centrifuged and the beads were washed twice for 10′ with phosphate buffered saline (PBS) before being resuspended in 1 ml PBS. Binding of EGFP-Tau was quantitative as judged by the loss of protein (280 nm) and EGFP (488 nm) absorbance in the supernatant of the reaction mixture. The resulting EGFP-Tau silica beads were stained mainly at the surface and their fluorescence intensities were comparable to typical (transiently expressed) EGFP levels in experiments on mammalian cells. Laser power and detector gains in the imaging experiments were similar to those used in biological samples.

For Cy3 labeling of the conjugated EGFP-Tau, the pellet of 100 μl aliquots of the protein-coated particles was resuspended in 50 μl bicine buffer and was stained with varying concentrations of Cy3 monofunctional reactive dye (Amersham Biosciences Europe GmbH, Freiburg, Germany) from a 10 mM stock solution in dry dimethylformamide. The labeling reactions were inverted continuously for 30′ allowing a homogeneous conjugation of the protein with Cy3 dye. The samples were finally washed several times with PBS to remove unconjugated dye and were resuspended in PBS. From the labeling titration experiment, the sample labeled with 40 μM of Cy3 reactive dye was found to result in an average labeling ratio of 2 Cy3/EGFP with an average FRET efficiency of ~30% (as detected in the frequency domain). This preparation was chosen for the lifetime experiments because its FRET efficiency represents a realistic value that we frequently observe in biological samples.

EYFP-I148V was generated by site-directed mutagenesis. EYFP and its mutant EYFP-I148V were purified as described for the EGFP-Tau constructs. A 7-μl aliquot of EYFP/EYFP-I148V mixtures with different relative fractions of the two mutants were loaded in a 1536 multiwell plate for the imaging of their lifetime in solution.

Human SHSY-5Y neuroblastoma cells were transiently transfected with a vector encoding GPI-anchored EGFP. The cells were subsequently (M. O. Ruonala, D. van den Heuvel, B. Gadella, A. J. Verkleij, H. C. Gerritsen, and P. M. P. van Bergen en Henegouwen, unpublished data) rinsed and incubated for 5′ with ice-cold binding medium (RPMI/25 mM Hepes/5% BSA) on ice. GM1 gangliosides were labeled by incubating the cells with 1 μg/ml of Alexa594 conjugated cholera toxin subunit-β in binding medium for 1 h on ice. The cells were rinsed four times for 5′ with ice-cold binding medium, and fixed with ice-cold 4% formaldehyde in PBS.

The EGFP-Tau silica beads, the EGFP-Tau-Cy3 FRET model beads, and the SHSY-5Y preparations were mounted on coverslips in Mowiol.

THEORY

In the analysis, a discrete lifetime distribution $M = [t_p, a_p(t_p)]$ is assumed in which a_p values are the weight parameters ($\sum_p \alpha_p = 1$) of each time decay. In the frequency domain, the measured phase-lag and demodulation factors are (8,25):

$$\phi = \arctan\left\{\left[\sum_p \alpha_p \left(1+\omega^2\tau_p^2\right)^{-1}\omega\tau_p\right] \Big/ \left[\sum_p \alpha_p \left(1+\omega^2\tau_p^2\right)^{-1}\right]\right\} \tag{2a}$$

$$m = \left\{\left[\sum_p \alpha_p \left(1+\omega^2\tau_p^2\right)^{-1}\omega\tau_p\right]^2 + \left[\sum_p \alpha_p \left(1+\omega^2\tau_p^2\right)^{-1}\right]^2\right\}^{\frac{1}{2}} \tag{2b}$$

$$\tau_\phi = \omega^{-1}\tan\phi; \quad \tau_m = \omega^{-1}(m^{-2}-1)^{\frac{1}{2}}, \tag{2c, d}$$

in which ω is the circular frequency. Equations 2c and 2d demonstrate the dependence of the phase-lag and demodulation on the lifetimes.

To simplify the formalism, it is possible to substitute the following quantities:

$$x_p = \omega\tau_p; \quad y_p = \alpha_p \Big/ \left(1+x_p^2\right), \tag{3a, b}$$

with which we can write:

$$\begin{aligned} \phi &= \arctan\left[\left(\sum_p y_p x_p\right) \Big/ \left(\sum_p y_p\right)\right]; \\ m &= \left[\left(\sum_p y_p x_p\right)^2 + \left(\sum_p y_p\right)^2\right]^{\frac{1}{2}}, \end{aligned} \tag{4a, b}$$

where $y = [x_p, y_p(x_p)]$ represents the distribution of the weighed and normalized lifetime components. In general, the moment of a distribution is defined as:

$$i_n = \sum_p y_p x_p^n. \tag{5}$$

The first moment of a distribution is its mean value (μ) whereas the variance (σ) is the second moment (I_2) centered on the mean ($\sigma^2 = I_2 - \mu^2$). It becomes clear by comparing Eqs. 5 and 4a,b that the phase-lag and the demodulation factors can be expressed in terms of moments of the distribution y. Combining these relations and rewriting Eqs. 2c and 2d in the moment formalism, we obtain:

$$x_\phi = i_1/i_0 = I_1; \quad x_m = \left[\left(i_0^2 + i_1^2\right)^{-1} - 1\right]^{\frac{1}{2}}. \tag{6a, b}$$

I_1 is the first moment of the new distribution $Y = [x_p, y_p(x_p)/i_0]$. In other words, the phase lifetime estimation represents the average value of Y. The meaning of the lifetime retrieved from the demodulation is less obvious. For distributions like M and y it is straightforward to demonstrate (see Theorem 1 in Supplementary Material) that:

$$M_n = i_n + i_{n+2} \forall n \geq 0 \Rightarrow (n = 0), i_2 = 1 - i_0. \quad (7)$$

This is the relation between the nth moment of the M distribution and the nth and $(n + 2)$th moments of the distribution y. The relation between i_0 and i_2 (Eq. 7, $n = 0$) allows writing (see Supplementary Material):

$$x_m = \left\{ \left[I_2(2 + I_2) - I_1^2 \right] \Big/ \left[1 + I_1^2 \right] \right\}^{\frac{1}{2}}. \quad (8)$$

And therefore:

$$\begin{cases} I_1 \equiv \mu; \\ I_2 \equiv \sigma^2 + \mu^2 \end{cases} \Rightarrow \begin{cases} x_\phi = \mu \\ x_m = \left\{ \mu^2 + \sigma^2 \left[\sigma^2 (1 + \mu^2)^{-1} + 2 \right] \right\}^{\frac{1}{2}}. \end{cases} \quad (9a, b)$$

Equation 9b shows the relation between the measured phase lifetime, the demodulation lifetime, and the lifetime distribution. They demonstrate that: i), the phase lifetime estimation is equal to the weighed mean lifetime whose distribution is Y; and ii), the modulation lifetime estimation is greater than the phase lifetime estimation and diverges as the distribution becomes more heterogeneous.

This agrees with experimental data and with the commonly accepted interpretation of the discrepancy between the two estimations.

Furthermore, this formalism allows the quantification of the heterogeneity of the distribution. It is possible to further simplify the formalism by writing:

$$x_m \approx (\mu^2 + 2\sigma^2)^{\frac{1}{2}}, \quad (10)$$

this approximation holds for a coefficient of variation of the distribution ($CV = \sigma\mu^{-1}$) that is <1 (see Results). It is therefore possible to derive a heterogeneity estimator based on measured x_m and x_ϕ:

$$x_m^2 - x_\phi^2 = 2\sigma^2 \left\{ 1 + \sigma^2 \left[2(1 + \mu^2) \right]^{-1} \right\} \approx 2\sigma^2, \quad (11)$$

in which both the exact and approximated relations are shown. The variance, the CV, and the second moment of the lifetime distributions can thus be estimated by:

$$\sigma \approx \left[\frac{1}{2} \left(x_m^2 - x_\phi^2 \right) \right]^{\frac{1}{2}}; \quad CV \approx x_\phi^{-1} \left[\frac{1}{2} \left(x_m^2 - x_\phi^2 \right) \right]^{\frac{1}{2}}$$
$$I_2 \approx \frac{1}{2} \left(x_m^2 + x_\phi^2 \right). \quad (12a, b, c)$$

Furthermore, in the presence of only two lifetimes, it is possible to derive the linear relationship between the second and the first moment of the lifetime distribution of a two-lifetime (x_1,x_2) system (see Theorem 2 in Supplementary Material):

$$I_2 = (x_1 + x_2)\mu - x_1 x_2. \quad (13)$$

This is an intrinsic property of the lifetime distribution weighing in frequency-domain detection. It physically explains the meaning of single-frequency measurement-based global analysis and its linear graphical representation (see Results).

Equation 9b and the approximations Eqs. 10 and 13 present the main results of this work and allow application of lifetime heterogeneities to be used in FD-FLIM data analysis.

Furthermore, comparing Eqs. 1 and 6 it becomes clear that:

$$i_0 = F_{cos} F_{DC}^{-1}; \quad i_1 = F_{sin} F_{DC}^{-1}. \quad (14a, b)$$

Equation 14a,b and the relation between the zeroth and second moments of the lifetime distribution (see Theorem 1 in Supplementary Material) allow the derivation of a simple relation that links the normalized second moment of the lifetime distribution with the Fourier coefficients:

$$I_2 = i_0^{-1} - 1 = F_{DC} F_{cos}^{-1} - 1. \quad (15)$$

By comparing Eqs. 1, 14, and 15 it is clear that the noise in the second moment estimation is in the same order of magnitude as the phase lifetime noise, and less than the error in the computation of the modulation lifetime estimation. The second moment can be directly calculated from the experimental data using Eq. 15 or approximated using Eq. 12c.

RESULTS

Lifetime heterogeneity resolution

The fluorescence lifetime heterogeneity is commonly quantified by the difference between the phase- and the modulation-lifetime estimations in FD-FLIM at a single modulation frequency. Equation 11 presents a quantitative estimator for lifetime distributions without the assumption of particular distributions.

The LiMA of a two-component system is instructive because it highlights several properties of the method. The generalization to multicomponent systems is straightforward. However, the analytical study of continuous distributions is somewhat complicated by difficulties in computing integrals. For this reason we here employed numerical integrations. Fig. 1 *A* shows the true fluorescence lifetime population (M) used for simulations, which are carried out at a modulation frequency equal to 80 MHz. The two lifetime distributions are centered at 3.0 and 2.0 ns and with standard deviations equal to 0.75 and 1 ns, respectively. The relative fraction of the shorter component is varied between 0 and 100% in 10 steps, to investigate the behavior of the lifetime heterogeneity. The simulated data sets were noise-free. Fig. 1 *B* shows true standard deviation of the discrete fluorescence

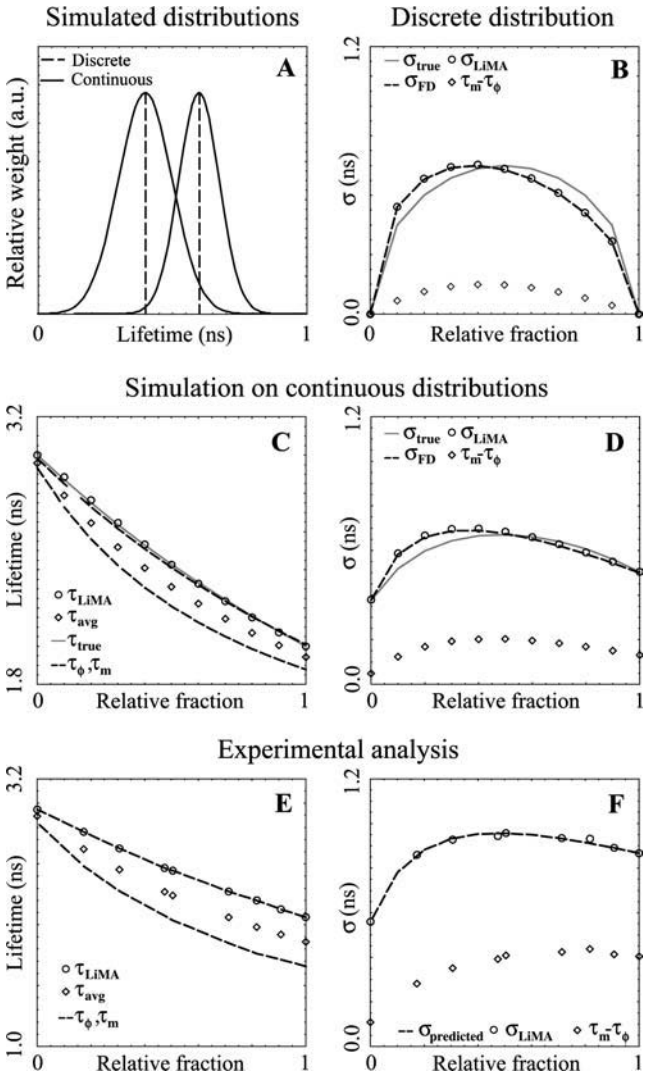

FIGURE 1 Lifetime heterogeneity for two-component discrete, continuous, and experimental systems. Panel *A* shows a two-component system with discrete lifetime components (*dashed lines*) of 2.0 and 3.0 ns, respectively, and a system with two continuous Gaussian lifetime distributions of different width centered around the same lifetimes (continuous lines, $CV = 50\%$ and $CV = 25\%$ for the 2- and 3-ns component, respectively). Panels *B*, *D*, and *F* show the standard deviation of the distributions obtained by mixing the two components with a relative fraction of 0% (only the longer component) to 100% in steps of 10%. The standard deviation of the true lifetime distribution (*M*, *gray solid line*), the standard deviations as computed by LiMA in its complete (Eq. 15, *dashed line*) and approximate form (Eq. 11a; ○) are shown. The difference of the phase- and modulation-lifetime estimations is represented by diamonds, and represents a frequently used heterogeneity estimator. Panels *C* and *E* show the phase- and modulation-lifetime estimations (*dashed lines*, τ_m is always greater than τ_ϕ) and their average (◇). The true average lifetime (*gray solid line*) is in good agreement with the values computed with LiMA (○). Panels *E* and *F* show the experimental results from the lifetime determination of a mixture of two different EYFP mutants exhibiting lifetimes of ~2- and ~3-ns and widths (*CV*) of ~50 and ~20%, respectively. Dashed lines represent τ_ϕ, τ_m (*E*) and the standard deviation (*F*) for the different relative fractions that were predicted from measurements of the two unmixed EYFP mutant components. The lifetime and standard deviation calculated by LiMA are in good agreement with the predicted values.

lifetime distribution (*gray solid line*), the LiMA-based standard deviation using Eq. 15 (*dashed line*), and the approximate LiMA estimator (Eq. 11a; *circles*). Fig. 1 *D* shows the same simulations for the two Gaussian lifetime distributions.

The arithmetic difference of the phase and modulation lifetimes is commonly used as heterogeneity estimator (Fig. 1, *B*, *D*, and *F*; *squares*). This enables only a qualitative understanding of lifetime heterogeneities, whereas the LiMA heterogeneity estimator correctly retrieves the lifetime heterogeneity. The mismatch with the true lifetime heterogeneity is due to the intrinsic weighing of the FD detection.

Fig. 1 *C* shows lifetime estimations computed with the Gaussian distribution. The bottom and top dashed curves represent the phase- and modulation-lifetime estimations, respectively, and their average is indicated by squares. The real average lifetime (M_1), computed from the true lifetime distribution (*gray solid line*) approximates the modulation lifetime, because of the simulated high heterogeneity. In general, the real average lifetime will lie between the two measured fluorescent lifetimes. The Gaussian distributions are positively skewed by the frequency-domain weighing factors *y*. If, however, pure Gaussian distributions are assumed than the average and standard deviation can be conveniently described by the moments of the Gaussian distributions. Using Gaussian distributions together with Eq. 7 ($n = 1$) and Eq. 15, the following expression for the true average lifetime estimator (τ_{best}) can be derived (see Supplementary Material):

$$\tau_{best} = \tau_\phi\left[1 + 2\sigma^2(1 + I_2)^{-1}\right]. \quad (16)$$

Fig. 1 *C* shows this estimator (*circles*); Eq. 16 holds for Gaussian distribution and for coefficient of variation <1 (see Supplementary Material). Different assumptions regarding the distributions will result in different relationships and estimators.

Fig. 1, *E* and *F*, shows the same quantities as in panels *C* and *D*, but now on experimental data. Two EYFP mutants were mixed to vary the average lifetime and its heterogeneity. EYFP has an average lifetime of ~2.9 ns with a width of ~0.6 ns as estimated by LiMA. EYFP-I148V exhibits a reduced lifetime (~1.9 ns) and an increased heterogeneity (~0.9 ns). The experimental data (Fig. 1, *E* and *F*) follow the same behavior as the simulations (Fig. 1, *C* and *D*). Furthermore, by the use of reference lifetime values measured in the presence of only a single component, it is possible to predict the lifetime heterogeneity as a function of the relative fraction of the two mutants (*F*, *dashed line*). The LiMA heterogeneity estimator (*F*, *squares*) is in excellent agreement with the experimental data, thereby demonstrating the validity of the models.

LiMA on pixel ensembles: a two-component system

LiMA can be performed on the complete pixel ensemble under the assumption of spatially invariant lifetimes.

Defining:

$$\begin{cases} a = x_1 + x_2 \\ b = x_1 x_2 \end{cases}, \tag{17}$$

it is possible to write, on a pixel-by-pixel (p,q) basis, the following relationship for a two-component system:

$$I_2[p,q] = a x_\phi[p,q] - b. \tag{18}$$

The second moment depends linearly on the mean lifetime so that I_2 can be plotted versus x_ϕ for each pixel and the obtained distribution can be fitted with a linear model. The fitting parameters a and b are the sum and the product of the two lifetime components, respectively, and they can be inverted to obtain:

$$x_{1,2} = \frac{1}{2}\left[a \pm (a^2 - 4b)^{\frac{1}{2}}\right], \tag{19}$$

where x_2 is the smaller (faster) component. Because x_ϕ is again the average of x with the distribution Y, the fraction map of each component can be built with the two resolved lifetime components according to the following formula:

$$\alpha_1 = (\mu - x_2)\left(1 + x_1^2\right)[(x_1 - x_2)(1 + I_2)]^{-1}. \tag{20}$$

Equation 20 is obtained by inversion of Eq. 6a, substitution of the moment definitions, and by using Eq. 7. Renormalization of the fractions by their quantum yields and correcting for the wavelength-dependent instrument response yields the true molecular fractions of both species.

Fig. 2 shows the application of LiMA to a simulated pixel ensemble. The simulation was performed on a 48 × 48 two-dimensional pattern with a gradient of populations as shown in inset *A*. The bottom left corner (*black*) represents a point in which only the slow component (set to 2.5 ns) is present, whereas the top right part of the pattern (*white*) only contains the fast component (1.0 ns). Using these two lifetimes and relative fractions, an eight-image phase-stack was generated. Poissonian noise was injected at a phase-dependent level corresponding to an average count of 8000 counts per pixel. This means that the average image of the phase-stack has ~8000 counts per pixel.

The inset *B* of Fig. 2 shows the pattern obtained for the simulation at a modulation frequency of 80 MHz. The reliability of the frequency-domain analysis and the amount of fluorescence signal required to realize a specific accuracy in the lifetime depends on the ratio of the lifetimes and the modulation frequency (36). To verify the effect of the modulation frequency on the analyses we ran simulations from 10 to 100 MHz in 100 steps to represent the typical FLIM

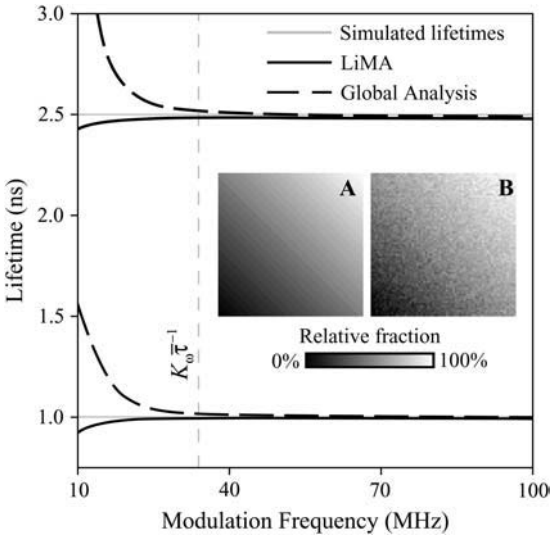

FIGURE 2 Comparison of solutions of a two-component lifetime system (2.5 and 1.5 ns) by global (*dashed line*) and moment (*solid line*) analysis as a function of modulation frequency. The simulations are carried out without data weighing at a modulation frequency of 80 MHz. GA is slightly more accurate at higher frequencies but diverges faster than LiMA at low frequencies. Below ~40 MHz, both analysis methods diverge as both models fail. This point matches with the limiting modulation frequency for correct estimation of lifetimes as predicted by LiMA (*dashed vertical gray line*). Inset *A* shows the simulated pattern where the relative fraction (A_1) of the 1.5-ns component is varied from 0 to 100%. Inset *B* shows the corresponding LiMA estimation that correctly retrieves the simulated pattern. When LiMA analysis is performed with data weighing, similar results are obtained but without the slight underestimation present in the nonweighed data (not shown).

experimental region. The graph in Fig. 2 shows the estimations of the simulated two lifetime components—using global analysis (*dashed line*, using the graphical algorithm) and LiMA (*solid black curve*). Both methods yield accurate lifetime values (*solid gray lines*) at sufficiently high modulation frequencies. At very high modulation frequencies (>100 MHz, data not shown) both methods yield a small underestimation of the two lifetimes. The curves shown in Fig. 2 are the average of 50 simulation runs. Simulations with different lifetimes, photon counts, phase-steps, and data weighing yielded consistent results.

Lifetime moment and global analysis

In recent years, global analysis has been applied to the interpretation of multifrequency and single-frequency (30,31) FLIM data. The GA algorithm applied to single-frequency data minimizes:

$$\chi^2(\tau_1,\tau_2,\alpha_{1,i}) = \sum_{i=1}^{N}\left\{\begin{array}{c} \sigma_{A,i}^{-2}\left[A_i - \omega\tau_1\alpha_{1,i}\left(1+\omega^2\tau_1^2\right)^{-1} - \omega\tau_2(1-\alpha_{1,i})\left(1+\omega^2\tau_2^2\right)^{-1}\right]^2 \\ + \sigma_{B,i}^{-2}\left[B_i - \alpha_{1,i}\left(1+\omega^2\tau_1^2\right)^{-1} - (1-\alpha_{1,i})\left(1+\omega^2\tau_2^2\right)^{-1}\right]^2 \end{array}\right\}, \tag{21}$$

where A and B are defined as:

$$A_i = M_i \sin(\Delta\phi_i); \quad B_i = M_i \cos(\Delta\phi_i) \tag{22a, b}$$

$$A_i = \sum_{q=1}^{Q} \omega\tau_q\alpha_{q,i}\left(1+\omega^2\tau_q^2\right)^{-1}; \quad B_i = \sum_{q=1}^{Q} \alpha_{q,i}\left(1+\omega^2\tau_q^2\right)^{-1}. \tag{22c, d}$$

These definitions match those of the zeroth and first moments. The χ^2 minimization in the global analysis fit thus serves to vary lifetime and relative population until the measured and calculated pixel-by-pixel moments match. This iterative minimization is carried out in LiMA by a linear fit.

Interestingly, the moment analyses allows us to estimate the minimum modulation circular frequency required for resolving two lifetimes in global analysis. Using Eq. 13 it is possible to estimate this frequency (see Supplementary Material):

$$\omega \geq K_\omega \bar{\tau}^{-1}, \tag{23}$$

with $\bar{\tau}$ being the average lifetime of the two components and K_ω a constant with value 0.375. In the example of Fig. 2, Eq. 23 yields a minimum modulation frequency of 34 MHz, a value consistent with the simulations. This value is congruent with the previous literature. In fact, the retrieval of the phase- and modulation-lifetime estimations is optimal for $K_\omega = 0.11$ and $K_\omega = 0.22$, respectively (36). However, this analysis did not deal with two-component systems.

During the writing of this article, a graphical FLIM analysis method for FD-FLIM data was published (32), in which a two-component system was analyzed by a linear fit of the FLIM data. The algorithms used earlier for single-frequency GA and for the linear regression of the fit are similar. The theoretical background and the physical quantities fitted in the LiMA and in the GA-derived statistical analysis are different. However, careful comparison between the two formalisms reveals the equivalence of the two methods.

The parameters fitted on a pixel-by-pixel [p,q] basis by Clayton and colleagues are A and B (Eqs. 22a,b and 22c,d). Here, the slope and offset are related to the two-lifetime components by:

$$\begin{aligned} A[p,q] &= u + vB[p,q]; \\ u &= [\omega(\tau_1+\tau_2)]^{-1}; \\ v &= (\omega^2\tau_1\tau_2 - 1)/[\omega(\tau_1+\tau_2)]. \end{aligned} \tag{24a, b, c}$$

The mathematical equivalence of LiMA and GA can be demonstrated using Eq. 18. To this end, the second moment and the phase lifetime need to be substituted by Eqs. 6 and 15. Renaming subsequently i_1,i_0 to B and A, gives:

$$A = a^{-1}[1 + (b-1)B], \tag{25}$$

from which the relation between the fit parameters u,v in Eq. 24a and the LIMA formalism becomes clear.

$$\begin{cases} u = a^{-1} \\ v = a^{-1}(b-1) \end{cases} \Rightarrow \tau_{1,2} = (2\omega u)^{-1}\left\{1 \pm [1-4u(u+v)]^{\frac{1}{2}}\right\} = (2\omega)^{-1}\left[a \pm (a^2-4b)^{\frac{1}{2}}\right]. \tag{26}$$

The moment formalism thus offers a complete theoretical understanding of the global analysis and provides additional powerful tools like the pixel-by-pixel heterogeneity estimator.

A comparison between moment (*solid line*) and global (*dashed curve*) analysis is also shown in Fig. 2. Here, no data weighing factor was taken into account in the fit procedures. Both methods allow the estimation of the simulated lifetime components (*solid lines*) down to the lower limit of the modulation frequency that no longer supports reliable detection of lifetimes. At higher frequencies both methods tend to give underestimations of the two real lifetimes.

The global analysis results appear better for higher modulation frequencies but diverge before LiMA in the lower frequency region. When data weighing is taken into account, GA and LiMA perform equally well. Both methods converge to the same lifetimes as in the nonweighed cases, but without the lifetime underestimation. Data weighing allows both methods to converge at better results, but at the cost of a less efficient implementation of the algorithms.

In the experimental comparison between LIMA and GA comparable correlation coefficients, standard errors, and χ^2 were obtained for the weighed fits.

A constrained two-component system FRET model

A two-component system exhibits three degrees of freedom; the two different lifetimes and the relative fraction of the two populations. In general it is theoretically and practically impossible to resolve the system on a pixel-by-pixel basis with a single-frequency measurement. However, in FRET efficiency measurements, it is possible to constrain the system and remove one degree of freedom (33). If we consider a donor fluorescent molecule with a constant lifetime τ_0, a fraction of donor molecules that exhibits FRET α and a FRET efficiency ε, the entire system is governed by two variables, α and ε. With only two degrees of freedom, the mathematical problem is closed at each pixel location. Using the moment formalism α and ε can be solved:

$$\begin{cases} \alpha = \left\{I_2^2 + \mu^2 + \mu_0\left[\left(1+\mu^2\right)\mu_0 - 2\mu(1+I_2)\right]\right\}/ \\ \qquad \{(1+I_2)[I_2 + \mu_0(\mu_0 - 2\mu)]\} \\ \varepsilon = 1 - [I_2\mu_0^{-1} - \mu]/[(\mu - \mu_0)] \end{cases} \tag{27a, b}$$

Understanding of the error propagation of α and ε is useful for a proper data interpretation. Using the moment formalism, it is possible to arrive at an analytical description of the minimal FRET fraction and FRET efficiency that produce statistically significant estimations. To visualize the effect of the noise in the lifetime detection on the estimation of α and ε, we simulated an eight-image phase-stack of a 2.5-ns lifetime fluorochrome, at a modulation frequency equal to 80 MHz. Here, Poissonian noise was injected as described before at an average count of 1000 and 16,000 photons per pixel. With these parameters, the simulated phase and

modulation lifetimes exhibit coefficients of variations >4 and 1%, respectively, values that are achieved in practice with biological samples in our setup.

The results are presented in Fig. 3 in which FRET fraction (*top row*) and efficiency (*middle row*) patterns of 48 × 48 pixels are plotted. These two-dimensional distributions map all possible combinations of populations and efficiencies. The simulated patterns before noise addition are shown in the right column. The bottom row presents the average (FRET efficiency and fraction) percentage deviation of the estimated patterns from the ideal case and thus represents the goodness of the constrained model. For all patterns shown in Fig. 3, black represents 100% and white 0%. The noise in the results is caused by the Poissonian noise that is injected into the simulated experimental conditions. The model only fails under conditions close to a single component situation, i.e., in the absence of a species ($\alpha = 0$ and/or $\varepsilon = 0$) that undergoes FRET, causing deviations equal to or greater than unity. These are pixels with a lifetime close to the non-FRET species.

The analytical study of the errors in the estimation of α and ε is complicated. However, by using Eq. 12a,b,c it is possible to simplify the formalism and to obtain the limiting solutions ($\alpha \rightarrow 0$, $\varepsilon^2 \rightarrow 0$). It can be shown that the errors diverge to infinity as:

$$CV_\tau \alpha^{-1} \varepsilon^{-2}, \tag{28a}$$

where CV_τ is the coefficient of variation of the measured lifetime.

Equation 28a can be used to plot the constant noise contours shown in Fig. 3 (*bottom row*):

$$\alpha \varepsilon^2 = K_{\text{noise}} CV_\tau. \tag{28b}$$

K_{noise} is the factor that allows the parameterization of the iso-noise curves. The bottom panels of Fig. 3 show the plots of Eq. 28b with $K_{\text{noise}} = 1$ (*white dashed line*) and $K_{\text{noise}} = 0.1$ (*black dashed line*). The first line ($K_{\text{noise}} = 1$) separates the (ε,α) plane in regions in which the system cannot be solved (lower values of ε and α) and where the estimates of FRET efficiency and fraction converge to the simulated values (higher values of ε and α). This allows one to estimate that, under the conditions of the simulations, minimal FRET efficiencies in the range of 10–20% are required to resolve the FRET population. This is a realistic level under normal experimental conditions. The limits to the fraction size of the species that exhibit FRET are less strict. These limits can be obtained by using Eq. 28b with $K_{\text{noise}} = 1$:

$$\varepsilon_{\text{limit}} = CV_\tau^{\frac{1}{2}}; \quad \alpha_{\text{limit}} = CV_\tau. \tag{28c}$$

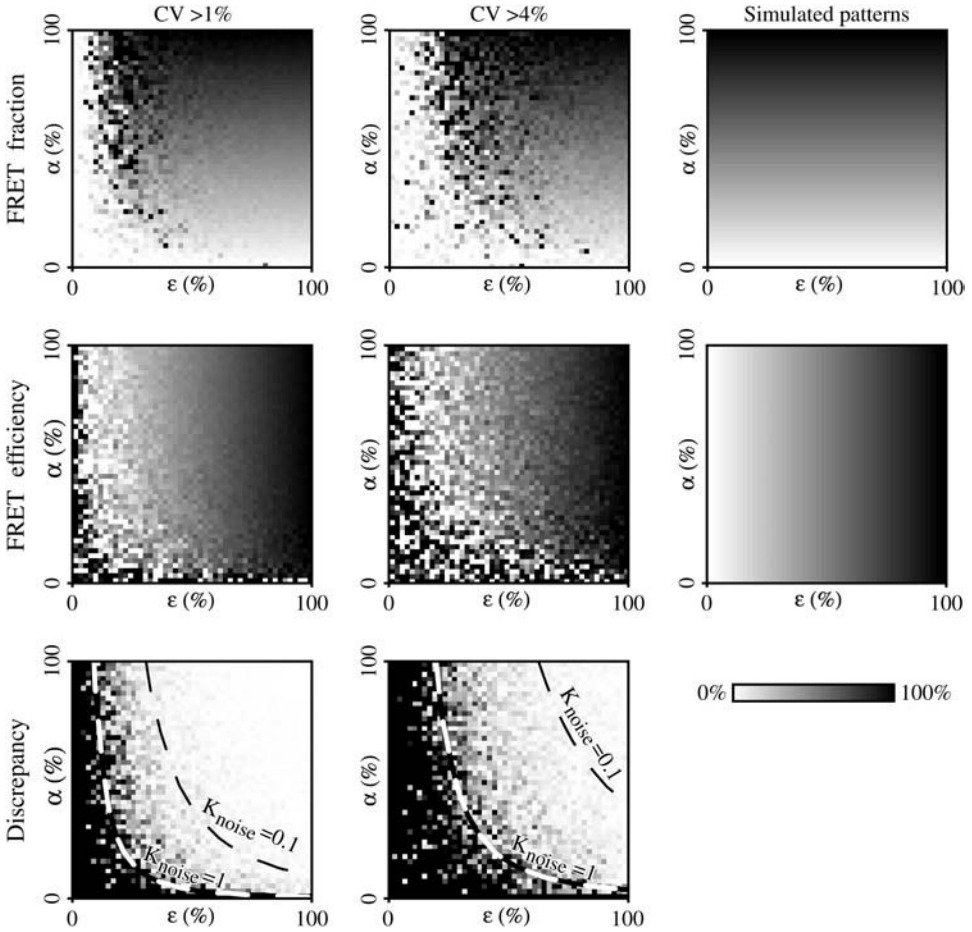

FIGURE 3 Simulation of a constrained two-component FRET system with added Poissonian noise. The coefficient of variation in the lifetime (CV_τ) is >1% for the results presented in the left column and 4% in the middle column. The first and second rows show the fraction of molecules undergoing FRET (α, FRET fraction) and the FRET efficiency (ε), respectively. These values were estimated from the analytical solution of the constrained two-component system. The original simulated patterns before the addition of noise are shown in the right column. In all panels, black and white indicate 100 and 0%, respectively. The gradients are only partially resolved due to the noise content. The noise in the estimations increases at low FRET efficiencies and FRET fractions. This is emphasized in the bottom row that shows the average absolute difference between the simulated α and ε and their estimated values in the constrained two-component system analysis. The curves represent lines of equal noise as derived by LiMA (see text for a detailed description). The white dashed line ($K_{\text{noise}} = 1$) represents the limit of convergence of the technique. Higher (ε,α) values are necessary to obtain statistically significant estimations.

The lifetime noise content (36,37) can be measured and related to the detected number of photons (N) resulting in a figure of merit (FoM) of the detection system ($CV_\tau = FoM\, N^{-1/2}$).

The analytical solution of this FRET model (33), presented in the moment formalism by Eq. 27, is based on the assumption of discrete lifetime distributions. Lifetime heterogeneity invalidates the model and limits its applicability. Fig. 4 (*bottom panel*) shows a simulation of such a FRET model with a control (no acceptor present) lifetime of 2.5 ns and 30% (CV) heterogeneity. For the short (FRET) lifetime the same heterogeneity was used. Three FRET efficiencies were simulated: 30% (*blue lines*), 50% (*green lines*), and 70% (*red lines*). These values were kept constant while changing the fraction of molecules that exhibit FRET from 0 to 100%. The results of the analytical solution (*dashed lines*) presented above do not match the simulated FRET efficiencies in the presence of heterogeneity. Furthermore, these estimations show a high degree of correlation with the fraction of molecules that undergo FRET, a noticeable trend to overestimate the FRET efficiency and a marked divergence toward FRET efficiencies exceeding 100%.

In a control experiment (only donor) it is possible to measure both the average lifetime and the lifetime heterogeneity. We derived an analytical solution that uses this information to correct for the donor heterogeneity contribution in the FRET efficiency estimation:

$$\begin{cases} \mu_C = \dfrac{i_1 - {}^{(c)}i_1}{i_0 - {}^{(c)}i_0} \\ \varepsilon_{best} = 1 + \dfrac{\omega\tau_{best\text{-}ctrl}\mu_C - 1}{\omega\tau_{best\text{-}ctrl}(\mu_C + \omega\tau_{best\text{-}ctrl})} \end{cases}. \qquad (29a, b)$$

Where $\tau_{best\text{-}ctrl}$ is the control lifetime obtained from Eq. 16, i_0 and i_1 the moments of the sample lifetime, and ${}^{(c)}i_0$ and ${}^{(c)}i_1$ the moments measured on the control. Here, μ_C does not represent a lifetime estimator anymore but a parameter that, together with Eq. 29b, allows estimation of the real FRET efficiencies. These corrections do not require more control experiments than in typical FRET measurement. As shown in the simulation in Fig. 4 (*solid lines*), this estimator faithfully reproduces the simulated FRET efficiencies. A thorough description of the derivation of Eq. 29 is presented in the Supplementary Material.

However, the LiMA FRET efficiency estimator does not take into account the lifetime heterogeneity of the FRET component. At high heterogeneities ($CV > 50\%$) this causes an underestimation of the FRET efficiency (data not shown). However, at all levels of heterogeneity, the LiMA FRET estimator eliminates the erroneous correlation with the fraction of molecules undergoing FRET, and returns interpretable quantitative results.

The new LiMA-based estimators (Eqs. 16 and 29) were tested in a biological model. Human SHSY-5Y neuroblastoma cells expressing a GPI-anchored EGFP were incubated with CholeraToxin-Alexa594. The GPI modification targets

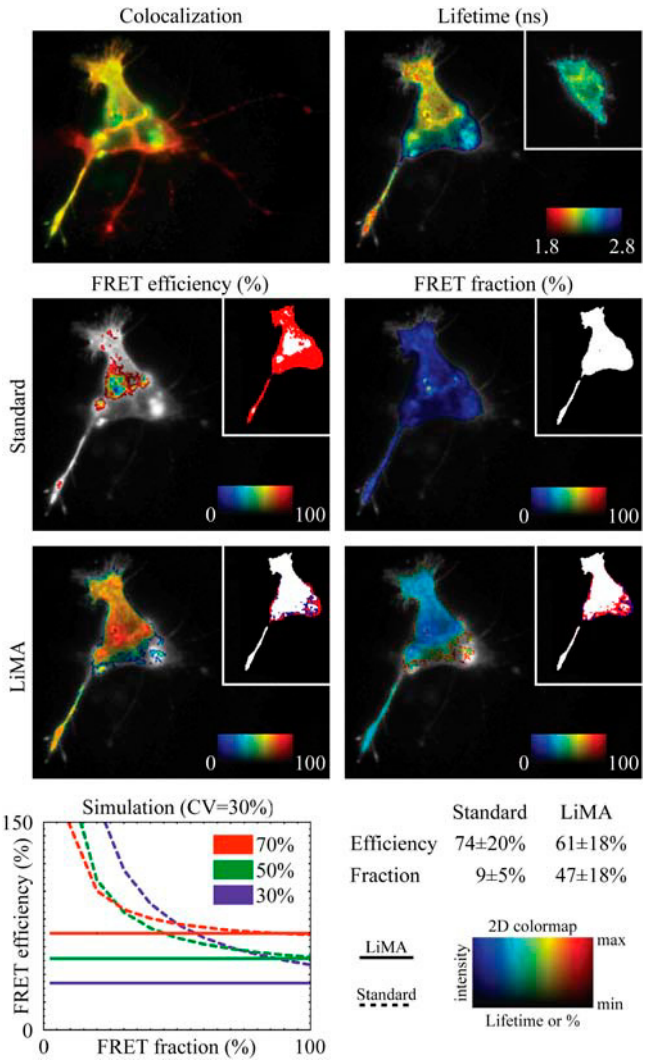

FIGURE 4 Biological application of the LiMA FRET estimator. Human SHSY-5Y neuroblastoma cells were transiently transfected with GPI-anchored EGFP (*green* in *colocalization* panel) construct and incubated with CholeraToxin-Alexa594 (*red* in *colocalization* panel). The donor lifetime map of the cell exhibiting extensive colocalization (*yellow* color) reveals areas with significant FRET (low lifetimes, *warmer colors*). The inset shows a cell that was not incubated with the CholeraToxin-Alexa594 FRET acceptor exhibiting control donor lifetimes. The standard algorithm (*second row*) for the determination of FRET population and efficiency does not converge to a solution. The LiMA FRET estimator (*third row*), takes lifetime heterogeneity into account, and allows the estimation of the FRET efficiency and fraction over most of the cell. The insets in the second and third panel show the regions in which both methods give physically relevant results (*white*) as defined by FRET efficiencies and fractions above 0% and below 100%, and regions in which the methods fail (*blue* <0% and *red* >100%). The estimations are overlayed with the intensity image for morphological comparison. The lower panel shows simulations that are performed with a heterogeneity of 30% that show how the LiMA FRET estimator (*solid lines*) compares with the standard analysis (*dashed lines*). Simulations were carried out for FRET efficiencies equal to 30% (*blue*), 50% (*green*), and 70% (*red*).

the EGFP to outer-membrane lipid microdomains, also known as lipid rafts. The cholera toxin binds to GM1 gangliosides that may be incorporated into the same microdomains. Their simultaneous recruitment in the same microdomain is expected to result in FRET between the two fluorophores (38,39).

Fig. 4 shows (*top row*) the colocalization of the two raft-resident probes and the average EGFP lifetime map obtained by FD-FLIM. The upper cell in the cluster exhibits reduced lifetimes due to FRET.

The analytical solution described by (33) and the moment formalism given by Eq. 27 cannot resolve the FRET efficiencies and fractions (Fig. 4, *middle row*).

The insets show the estimations that are above 100% (*red pixels*) and below 0% (*blue pixels*). In these regions, the results of the analyses have no physical meaning. The use of the LiMA estimators (Fig. 4, *bottom image row*) enables the quantification of the FRET efficiencies and the fraction of interacting molecules (61 ± 18 and 47 ± 18%, respectively). The model fails only in regions where the sample does not undergo FRET, i.e., in the lower two cells.

LiMA on fluorescent beads

To independently verify the relevance of the estimations of this theory, we measured the lifetimes of EGFP-conjugated silica beads with and without Cy3 labeling in the frequency domain and in the time domain. The FLIM instrumentations used differ considerably; FD-FLIM was performed using a wide-field microscope and TD-FLIM was performed using a laser scanning two-photon excitation microscope. The time-domain measurements served to produce ''independent'' reference lifetime values for the donor in the absence of the acceptor and in the presence of the acceptor. All the images were binned to obtain ~20,000 photons per pixel. The results of the comparison are summarized in Table 1. A single exponential fit of the time-domain data revealed a control EGFP lifetime of 1.97 ± 0.04 ns (mean ± SD), whereas stretched-exponential fitting yielded 1.90 ± 0.06 ns with a coefficient of variation of the distribution of 23 ± 8%. The average lifetime in the frequency domain was 1.95 ± 0.03 ns with a coefficient of variation estimated by LiMA of 36 ± 4%. In the control experiment, the spatially invariant approximation holds because of the presence of a single fluorochrome. However, in the frequency domain the moments analysis on the pixel statistical ensemble revealed a long lifetime component of 2.14 ± 0.03 ns (errors propagated from the experimental uncertainty), corresponding to the typical EGFP fluorescence lifetime, and a short (360 ± 5 ps) component. This is caused by a low but significant amount of background fluorescence that is not detected in the two-photon excitation time-domain measurements. The difference may be due to the difference in excitation mechanism and detection volume.

A bead exhibiting FRET is shown in Fig. 5. The top row presents the intensity images obtained using two-photon excitation single-photon counting and with single-photon excitation employing a charge-coupled device (CCD) camera. The acceptor fluorochrome was partially bleached on the right-hand half of the fluorescent particle using a 561-nm laser. Here a partial recovery of donor fluorescence can be observed as a result of a concomitant loss of FRET. The second row of Fig. 5 shows the average lifetime maps as measured in the time (*left*) and frequency (*right*) domain. The former lifetime map is computed by a constrained double-exponential fit. One of the two lifetimes was fixed at the control value.

The FD-FLIM lifetime map is the average of the phase and modulation lifetimes. The retrieved estimations of the FRET efficiency and fraction are presented in the two lower images (*left column*). The average lifetime in the time domain was 1.40 ± 0.10 and 1.65 ± 0.20 ns in the bleached and nonbleached areas, respectively. The FRET efficiencies were 56 ± 4 and 61 ± 10% and the relative populations were 52 ± 5 and 22 ± 4%, respectively. From this data, it is clear that photobleaching of the acceptor mainly affects the fraction of molecules that is involved in FRET and not the FRET efficiency.

The stretched-exponential fit of the TD data yielded estimations of the distribution broadness of 39 ± 8 and 27 ±

TABLE 1 Experimental comparison of TD- and FD-FLIM data analysis

	Lifetime (ns)		*CV* (%)		*CV* increase	
	TD	FD	TD	FD	TD	FD
Control	1.90 ± 0.06	1.95 ± 0.03	23 ± 8	36 ± 4	–	–
Bleached	1.40 ± 0.06	1.40 ± 0.03	39 ± 8	58 ± 3	1.7	1.6
Nonbleached	1.74 ± 0.06	1.64 ± 0.04	27 ± 10	50 ± 3	1.2	1.4

	ε (%)		α (%)	
	TD	FD	TD	FD
Bleached	56 ± 4	69 ± 3	52 ± 5	45 ± 3
Nonbleached	61 ± 10	71 ± 4	22 ± 4	28 ± 3

Average values refer to the fluorescent bead experiments of Fig. 5. The errors are presented as standard deviations.

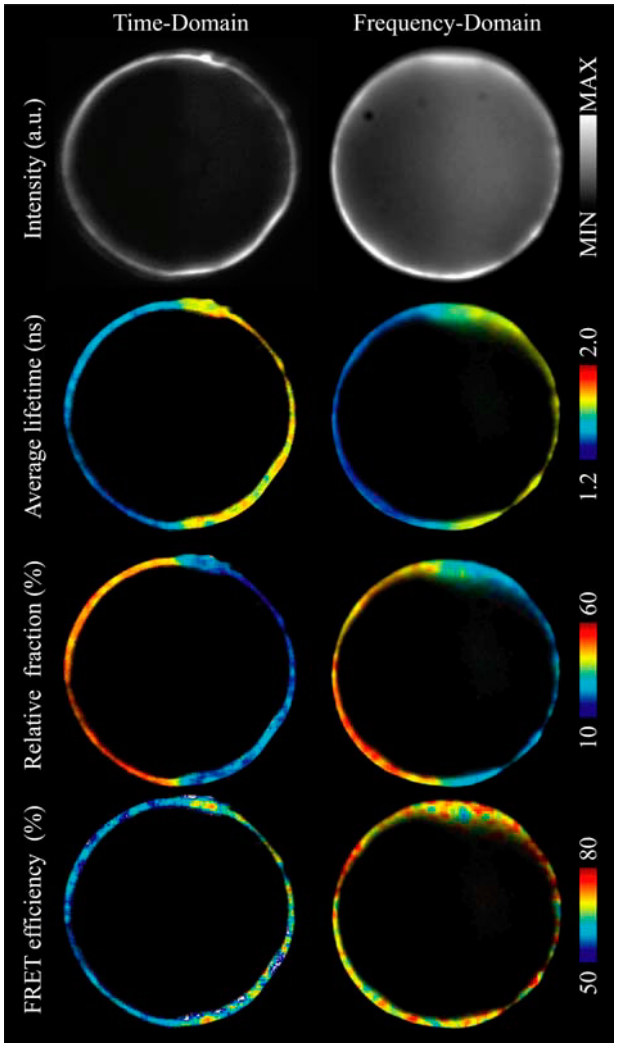

FIGURE 5 Comparison of time domain (*left column*) and frequency domain (*right column*) FLIM images of the same EGFP-Cy3 labeled silica beads. Silica beads were covalently conjugated with an EGFP-fusion protein that was subsequently labeled with Cy3 to constitute a defined FRET couple. The top images show the fluorescence intensity distributions of the EGFP donor acquired by single-photon counting, two-photon excitation imaging (*left*), and CCD camera-based wide-field imaging (*right*). The second row shows the corresponding average donor lifetimes measured in the time (*left*) and frequency (*right*) domain. Images of the fraction of molecules undergoing FRET (FRET fraction) and energy transfer efficiency are shown in the bottom two panels. These parameters were retrieved by standard fitting of a constrained biexponential decay in the time domain and by LiMA in the frequency-domain experiment. All results are shown in false color representation; ranges are indicated in the color bars.

10% (coefficient of variation) and lifetimes of 1.40 ± 0.06 and 1.74 ± 0.06 ns. Even though the broadness estimator is relatively noisy, it reveals a higher heterogeneity in the nonbleached region caused by a more heterogeneous mixture of molecules with respect to the control situation (23 ± 8%), i.e., molecules that exhibit FRET and those that do not.

The FD pixel-by-pixel moments analysis (Fig. 5, *right column*), showed results consistent with the TD. The average lifetimes were 1.40 ± 0.03 and 1.64 ± 0.04 ns with a coefficient of variation retrieved by LiMA of 58 ± 3 and 50 ± 3% for the nonbleached and the bleached regions, respectively. This estimator again demonstrated higher heterogeneity with respect to the control case (36 ± 4%).

Both LiMA (FD) and the stretched exponentials (TD) analysis revealed an increase of 1.6–1.7-fold of the measured fluorescence lifetime heterogeneity due to the presence of FRET-induced multiple lifetimes. Furthermore, the LIMA-based FRET efficiencies in nonbleached and bleached regions were 69 ± 3 and 71 ± 4% with populations of 45 ± 3 and 28 ± 3%, respectively. Therefore, the frequency-domain results also indicated that the change in lifetime is mainly due to a modulation of the molecular fraction exhibiting FRET rather than of the energy transfer efficiency. The analysis showed that a spatially invariant two-component lifetime approximation can be applied in this case.

The two-component system can be analyzed by LiMA and global analysis fitting (Eqs. 18 and 24a) of the pixel ensemble (Fig. 6, *solid line*). The long and short lifetimes amount to 2.16 and 0.68 ns for LiMA, and 2.16/0.71 ns for GA; this is consistent with the presence of a single molecular FRET-state with an absolute energy transfer efficiency of ~70%. The slow decay component is statistically equal to the one retrieved by LiMA in the control sample. The LiMA correlation coefficient and standard error of the estimate are 0.98 and 0.013, respectively, and for the global analysis 0.90 and 0.012. The reduced χ^2 of the weighted fits is equal to 1.79 and 1.85 for GA and LiMA, respectively (see Data Analysis and Supplementary Material). Fig. 6 shows the moment (*top panel*) and the global analysis (*bottom panel*) fit of the data set (*gray circles*) presented in Fig. 5. The second and the first moments of the lifetime distribution are linearly dependent as predicted by the theory. A simulation (*black circles*), performed as previously described with an average photon count equal to 4000 and with a 20 × 20 pattern, is overlaid to the experimental points. The simulated data set was in excellent agreement with the experimental values.

DISCUSSION

Lifetime heterogeneity resolution

TD- and FD-FLIM can resolve, in principle, an arbitrary number of complex exponential decays. In practice, imaging in the frequency domain is usually performed at a single excitation modulation frequency and on a wide-field microscope. On the other hand, time-domain microscopes are often built around laser scanning microscopes and the collection of a sufficient number of photons to fit a double-exponential decay requires very long acquisition times with typical biological samples. Fitting with stretched exponentials seems to be a good alternative for time-resolved data; it allows the estimation of the average and variance of complex

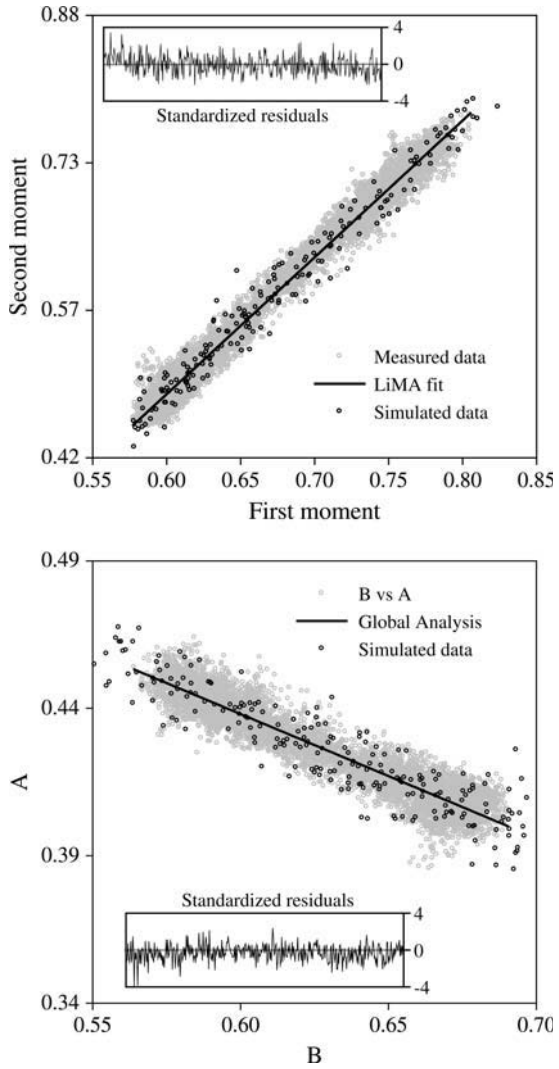

FIGURE 6 Moment and global analysis of the experimental data shown in Fig. 5. The top panel shows simulated data and the experimental data points for the experiment shown in Fig. 5, analyzed by LiMA (*top* panel) and global analysis. Linear fits (*solid black line*) of the experimental data (*gray open circles*) and simulated data (*black open circles*) are shown. The first and second moments of the lifetime distribution, as estimated by LiMA, are linearly dependent. This compares to the *A* and *B* parameters that are fitted by the GA algorithm. The simulations (*black open circles*) are in good agreement with the experimental data. The standardized fitting residuals of the experimental data for both methods are shown in the corresponding insets.

continuous lifetime distributions at comparatively low signal levels.

The introduction of the LiMA heterogeneity estimator for frequency-domain measurements offers an analogous advantage. Because this parameter refers to the weighted distribution of lifetimes, it is frequency dependent, but offers a quantitative estimator of the lifetime distribution broadness.

We demonstrated how the moment formalism can be used to define estimators for the average lifetime and for FRET efficiencies that minimize artifacts due to fluorescence lifetime heterogeneity. The heterogeneity analysis by LiMA is not restricted to discrete two-component lifetime systems but allows estimation of the width of any lifetime distribution.

Importantly, the coefficient of variation obtained by LiMA is compatible with all standard implementations of frequency-domain lifetime imaging. The average lifetime (or the newly defined estimator for the true average lifetime) in combination with the lifetime heterogeneity estimator and bidimensional histograms (τ_m plotted versus τ_ϕ) are a powerful method to present and analyze FD-FLIM data.

The model is validated by in vitro experiment and simulations. The heterogeneity can be predicted (Fig. 1 *F*, *dashed line*) by the use of control values ($\alpha = 0\%$ and $\alpha = 100\%$) and experimental observations (*circles*).

LiMA on the pixel ensemble

Global analysis of FD-FLIM data offers the possibility to extend quantitative measurements to multicomponent systems. Moreover, GA of single-frequency FD data is compatible with most FD setups.

We demonstrated that the lifetime moments analysis of the entire pixel ensemble is formally equivalent to the single-frequency global analysis approach. Previously, a different moments analysis framework was introduced by Weber (40) to investigate multifrequency data in the frequency domain. This formalism, however, cannot be extended to single-frequency measurements and is not related to the formalism presented here.

The LiMA formalism enables the complete understanding of global analysis at a single frequency. The LiMA algorithm fits $(F_{DC}F_{cos}^{-1} - 1)$ vs. $(F_{sin}F_{cos}^{-1})$, whereas the GA fits $(F_{sin}F_{DC}^{-1})$ vs. $(F_{cos}F_{DC}^{-1})$. The different noise sensitivities of these quantities cause a difference in robustness between the two fit procedures (Fig. 2).

At frequencies too high for reliable fluorescence lifetime detection ($\omega t > 1$), both methods underestimate the two lifetime components. The GA diverges to higher lifetime values at low frequencies, but it better approximates the global lifetimes at intermediate frequencies. In the same region, LiMA offers a slight underestimation of the real values. Overall, GA appears to be slightly more accurate, however, LiMA extends its window of high robustness to lower frequencies where GA rapidly loses reliability. Interestingly, the LIMA formalism allows estimating the minimal modulation frequency required to resolve a two-component system ($\omega t > 0.375$). Data weighing requires CPU expensive algorithms. LiMA seems to be more robust at high signal levels.

In our experiments LiMA turns out to be useful for on-line pixel-by-pixel and pixel ensemble analysis. Further data analysis can be carried out with both LiMA and GA (see www.quantitative-microscopy.org/pub/lima.html). The simulated data (Fig. 6, *black circles*) accurately matched the experimental data points (Fig. 6, *gray circles*) thereby validating the theoretical background and the previous simulations (Fig. 2).

A constrained two-component system FRET model

The analytical relation between the phase- and the modulation-lifetime estimation can be employed to analyze a constrained two-component system such as a FRET sample with a component (33) that exhibits FRET and a non-FRET component. The LiMA formalism offers the possibility of studying the applicability and reliability of two-component systems. In particular it allows estimating the minimal signal/noise ratio that is required to resolve the FRET efficiency and fraction. We showed how this method can be applied experimentally by comparing FD-FLIM LiMA with the results obtained from time-domain measurements and demonstrated how the results of the two techniques converge (Fig. 5 and Table 1). This method allows filling the gap between wide-field single-frequency FD-FLIM and time-correlated single-photon counting (or multiple-window time gating) TD-FLIM. Both methods require knowledge of the lifetime in the absence of FRET that can be easily obtained experimentally from a reference sample. Global analysis assumes spatially (and frequency) invariant lifetimes. For a sample that exhibits FRET with variable FRET efficiencies, this is not a reasonable assumption.

Furthermore, by avoiding iterative or multistep approaches, the analytical approaches such as LiMA allow fast (real-time) analysis of FD data. The pixel-by-pixel moments analysis allows the unambiguous discrimination between differences in intermolecular interactions and the amount of molecules that exhibit FRET versus those that do not exhibit FRET.

Finally, we introduced a model that takes into account, and corrects for, lifetime heterogeneity. The model allows the reliable retrieval of quantitative information on FRET efficiency and fraction.

It can be successfully applied in cases where the intrinsic heterogeneity of the donor lifetime or of the FRET process causes the previously reported analytical solution to fail, as shown in Fig. 4 for a biological application. The LiMA-based FRET estimator avoids artifacts connected to the departure from an ideal discrete two-component system. Furthermore, it allows the proper evaluation of intrinsically heterogeneous FRET pairs like, for instance, the popular CFP-YFP pair.

CONCLUSIONS

We introduced the moment formalism to analyze fluorescence lifetime data acquired in the frequency domain. So far this development elaborates on well-established data analysis methods for the frequency domain. However, other moments-analysis-based estimators may be developed that allow further refinement of the analysis of lifetime data. The main findings of this work are the analytical dependence of the phase and the modulation lifetimes on the lifetime heterogeneity and the linear relation between the second and the first moments of the FD weighted lifetime distributions. The latter explains single-frequency global analysis with physical quantities, allowing a better understanding of the method. The former enables the quantitative description of the lifetime heterogeneity. Furthermore this theoretical framework allows the analysis of errors for a FRET two-component system and for single-frequency global analysis. Previous attempts to obtain analytical solutions were unsuccessful. We demonstrated how, based on specific assumption of the lifetime distribution, the contribution of the lifetime heterogeneity to the error in the determination of, for instance, the average lifetime can be minimized.

More general, LiMA allows quantification of lifetime heterogeneity on a pixel-by-pixel basis without specific assumptions of the lifetime distribution. In this respect, LiMA can be used in the frequency domain in a similar way as stretched-exponential fits in time-domain data analysis. Furthermore, we introduced LiMA estimators for the average lifetime and the FRET efficiencies in heterogeneous systems in which previously defined estimators did not allow a proper quantification of these parameters.

In conclusion, lifetime moments analysis offers theoretical and practical tools for the understanding and quantification of fluorescence lifetime imaging microscopy data in the frequency domain.

SUPPLEMENTARY MATERIAL

An online supplement to this article can be found by visiting BJ Online at http://www.biophysj.org.

The authors thank Prof. Thomas J. Jovin for the critical reading of the manuscript and helpful discussions, Dr. Mika Ruonala for providing the SHSY-5Y GPI anchored GPI-GFP/CholeraToxin-Alexa594 sample, and Sundar Ganesan for supplying the purified EYFP and EYFP-I148V.

This work was supported by the DFG Research Center Molecular Physiology of the Brain.

REFERENCES

1. Gaviola, E. 1927. Ein Fluorometer. Apparat zur Messung von Fluoreszenzabklingungszeiten. *The European Physical Journal D-Atomic. Molecular and Optical Physics*. 42:853–861.
2. Spencer, R. D., and G. Weber. 1969. Measurements of subnanosecond fluorescence lifetimes with a cross-correlation phase fluorimeter. *Ann. N. Y. Acad. Sci.* 158:361–376.
3. Gratton, E., and M. Limkeman. 1983. A continuously variable frequency cross-correlation phase fluorometer with picosecond resolution. *Biophys. J.* 44:315–324.
4. O'Connor, D. V., and D. Phillips. 1984. Time Correlated Single Photon Counting. Academic Press, London, UK.
5. Wang, X. F., T. Uchida, and S. Minami. 1989. A fluorescence lifetime distribution measurement system based on phase-resolved detection using an image dissector tube. *Appl. Spectrosc.* 43:840–845.
6. Wang, X. F., T. Uchida, D. M. Coleman, and S. Minami. 1991. A 2-dimensional fluorescence lifetime imaging-system using a gated image intensifier. *Appl. Spectrosc.* 45:360–366.
7. Lakowicz, J. R., and K. W. Berndt. 1991. Lifetime-selective fluorescence imaging using an Rf phase-sensitive camera. *Rev. Sci. Instrum.* 62:1727–1734.

8. Gadella, T. W., Jr., T. M. Jovin, and R. M. Clegg. 1993. Fluorescence lifetime imaging microscopy (FLIM): spatial-resolution of microstructures on the nanosecond time-scale. *Biophys. Chem.* 48:221–239.

9. Morgan, C. G., A. C. Mitchell, and J. G. Murray. 1990. Nanosecond time-resolved fluorescence microscopy: principles and practice. *Trans. Roy. Microsc. Soc.* 1:463–466.

10. Bugiel, I., K. König, and H. Wabnitz. 1989. Investigation of cells by fluorescence laser scanning microscopy with subnanosecond time resolution. *Laser Life Sciences.* 3:1–7.

11. Ghiggino, K. P., M. R. Harris, and P. G. Spizzirri. 1992. Fluorescence lifetime measurements using a novel fiberoptic laser scanning confocal microscope. *Rev. Sci. Instrum.* 63:2999–3002.

12. Buurman, E. P., R. Sanders, A. Draaijer, H. C. Gerritsen, J. J. F. Vanveen, P. M. Houpt, and Y. K. Levine. 1992. Fluorescence lifetime imaging using a confocal laser scanning microscope. *Scanning.* 14:155–159.

13. So, P. T. C., T. French, W. M. Yu, K. M. Berland, C. Y. Dong, and E. Gratton. 1995. Time-resolved fluorescence microscopy using two-photon excitation. *Bioimaging.* 3:49–63.

14. Dong, C. Y., P. T. So, T. French, and E. Gratton. 1995. Fluorescence lifetime imaging by asynchronous pump-probe microscopy. *Biophys. J.* 69:2234–2242.

15. Carlsson, K., and A. Liljeborg. 1997. Confocal fluorescence microscopy using spectral and lifetime information to simultaneously record four fluorophores with high channel separation. *J. Microsc.* 185: 37–46.

16. Barzda, V., C. J. de Grauw, J. Vroom, F. J. Kleima, G. R. van, A. H. van, and H. C. Gerritsen. 2001. Fluorescence lifetime heterogeneity in aggregates of LHCII revealed by time-resolved microscopy. *Biophys. J* 81:538–546.

17. Treanor, B., P. M. Lanigan, K. Suhling, T. Schreiber, I. Munro, M. A. Neil, D. Phillips, D. M. Davis, and P. M. French. 2005. Imaging fluorescence lifetime heterogeneity applied to GFP-tagged MHC protein at an immunological synapse. *J. Microsc.* 217:36–43.

18. Förster, T. 1965. Delocalized excitation and excitation transfer. *In* Modern Quantum Chemistry. O. Sinanoglu, editor. Academic Press, New York, NY. 93–137.

19. Clegg, R. M. 1996. Fluorescence resonance energy transfer. *In* Fluorescence Imaging Spectroscopy and Microscopy. X. F. Wang and B. Herman, editors. John Wiley & Sons, London, UK. 180–252.

20. Gadella, T. W., Jr., and T. M. Jovin. 1995. Oligomerization of epidermal growth factor receptors on A431 cells studied by time-resolved fluorescence imaging microscopy. A stereochemical model for tyrosine kinase receptor activation. *J. Cell Biol.* 129:1543–58.

21. Bastiaens, P. I., and A. Squire. 1999. Fluorescence lifetime imaging microscopy: spatial resolution of biochemical processes in the cell. *Trends Cell Biol.* 9:48–52.

22. Wouters, F. S., P. J. Verveer, and P. I. Bastiaens. 2001. Imaging biochemistry inside cells. *Trends Cell Biol.* 11:203–211.

23. Esposito, A., and F. S. Wouters. 2004. Fluorescence lifetime imaging microscopy. *In* Current Protocols in Cell Biology. J. S. Bonifacino, M. Dasso, J. B. Harford, J. Lippincott-Schwartz, and K. M. Yamada, editors. John Wiley & Sons, New York, NY.

24. Lakowicz, J. R., H. Szmacinski, K. Nowaczyk, K. W. Berndt, and M. Johnson. 1992. Fluorescence lifetime imaging. *Anal. Biochem.* 202:316–330.

25. Clegg, R. M., and P. C. Schneider. 1996. Fluorescence lifetime-resolved imaging microscopy: a general description of lifetime-resolved imaging measurements. *In* Fluorescence Microscopy and Fluorescent Probes. J. Slavik, editor. Plenum Press, New York, NY. 15–33.

26. Lakowicz, J. R. 1999. Principles of Fluorescence Spectroscopy. Kluwer Academic/Plenum Publishers, New York, NY.

27. Murata, S., P. Herman, H. J. Lin, and J. R. Lakowicz. 2000. Fluorescence lifetime imaging of nuclear DNA: effect of fluorescence resonance energy transfer. *Cytometry.* 41:178–185.

28. Hanley, Q. S., V. Subramaniam, D. J. Arndt-Jovin, and T. M. Jovin. 2001. Fluorescence lifetime imaging: multi-point calibration, minimum resolvable differences, and artifact suppression. *Cytometry.* 43:248–260.

29. Lakowicz, J. R., and A. Balter. 1982. Theory of phase-modulation fluorescence spectroscopy for excited-state processes. *Biophys. Chem.* 16:99–115.

30. Verveer, P. J., A. Squire, and P. I. Bastiaens. 2000. Global analysis of fluorescence lifetime imaging microscopy data. *Biophys. J.* 78:2127–2137.

31. Verveer, P. J., and P. I. Bastiaens. 2003. Evaluation of global analysis algorithms for single frequency fluorescence lifetime imaging microscopy data. *J. Microsc.* 209:1–7.

32. Clayton, A. H., Q. S. Hanley, and P. J. Verveer. 2004. Graphical representation and multicomponent analysis of single-frequency fluorescence lifetime imaging microscopy data. *J. Microsc.* 213:1–5.

33. Gadella, T. W., Jr., R. M. Clegg, and T. M. Jovin. 1994. Fluorescence lifetime imaging microscopy: pixel-by-pixel analysis of phase-modulation data. *Bioimaging.* 2:139–159.

34. van Munster, E. B., and T. W. Gadella, Jr. 2004. Suppression of photobleaching-induced artifacts in frequency-domain FLIM by permutation of the recording order. *Cytometry A.* 58:185–194.

35. Lee, K. C. B., J. Siegel, S. E. D. Webb, S. Leveque-Fort, M. J. Cole, R. Jones, K. Dowling, M. J. Lever, and P. M. W. French. 2001. Application of the stretched exponential function to fluorescence lifetime imaging. *Biophys. J.* 81:1265–1274.

36. Philip, J., and K. Carlsson. 2003. Theoretical investigation of the signal-to-noise ratio in fluorescence lifetime imaging. *J. Opt. Soc. Am. A Opt. Image Sci. Vis.* 20:368–379.

37. Draaijer, A., R. Sanders, and H. C. Gerritsen. 1995. Fluorescence lifetime imaging, a new tool in confocal microscopy. *In* Handbook of Biological Confocal Microscopy. J. Pawley, editor. Plenum Press, New York, NY. 491–505.

38. Nichols, B. J. 2003. GM1-containing lipid rafts are depleted within clathrin-coated pits. *Curr. Biol.* 13:686–690.

39. Kusumi, A., I. Koyama-Honda, and K. Suzuki. 2004. Molecular dynamics and interactions for creation of stimulation-induced stabilized rafts from small unstable steady-state rafts. *Traffic.* 5:213–230.

40. Weber, G. 1981. Resolution of the fluorescence lifetimes in a heterogeneous system by phase and modulation measurements. *J. Phys. Chem.* 85:949–953.